ADVANCED FUNCTIONAL MATERIALS
www.afm-journal.de

Programmable Multi-Responsive Nanocellulose-Based Hydrogels With Embodied Logic

Beatriz Arsuffi, Gilberto Siqueira, Gustav Nyström, Silvia Titotto,* Tommaso Magrini,* and Chiara Daraio**

Programmable materials are desirable for a variety of functional applications that range from biomedical devices, actuators and soft robots to adaptive surfaces and deployable structures. However, current smart materials are often designed to respond to single stimuli (like temperature, humidity, or light). Here, a novel multi-stimuli-responsive composite is fabricated using direct ink writing (DIW) to enable programmability in both space and time and computation of logic operations. The composite hydrogels consist of double-network matrices of poly(*N*-isopropylacrylamide) (PNIPAM) or poly(acrylic acid) (PAA) and sodium alginate (SA) and are reinforced by a high content of cellulose nanocrystals (CNC) (14 wt%) and nanofibers (CNF) (1 wt%). These composites exhibit a simultaneously tunable response to external stimuli, such as temperature, pH, and ion concentration, enabling precise control over their swelling and shrinking behavior, shape, and mechanical properties over time. Bilayer hydrogel actuators are designed to display bidirectional bending in response to various stimuli scenarios. Finally, to leverage the multi-responsiveness and programmability of this new composite, Boolean algebra concepts are used to design and execute NOT, YES, OR, and AND logic gates, paving the way for self-actuating materials with embodied logic.

1. Introduction

Programmable materials are a novel class of materials that can self-actuate in response to external triggers, such as temperature, variations in pH, light intensity, as well as chemical, electric and magnetic fields. Such actuation must occur in a predictable manner, through controlled and gradual changes in physical and/or chemical properties.[1,2] In this context, responsive materials that can achieve a programmable shape transformation play a crucial role in the advancement of various fields including biomedical devices,[3] microfluidics,[4] and soft robotics.[5] However, while natural environments offer multiple stimuli at the same time, smart materials are often limited to respond to only one or two stimuli.[6,7] Furthermore, smart materials frequently lack precise temporal control over actuation, necessary for their full implementation for end-user applications.[8] Unlike smart materials, the design of programmable materials extends further than the conventional characterization of material properties. For example, if-then relationships, feedback mechanisms, information processing tools, and logic operations can be used to introduce varying degrees of intelligence into the material system, enabling the programmability and control of its entire behavior through adaptable strategies.[9–11] Materials with embodied logic generate predictable outputs in response to mechanical or chemical inputs, enabling materials-driven computation tailored to the specific physics and timescales of the target application.[12–15]

Hydrogels are among the most promising programmable materials that are used for conducting logic operations.[16–18] Hydrogels are hydrophilic polymeric materials with crosslinks between the chains, forming a 3-D network structure.[19,20] In contact with water or aqueous solutions, hydrogels can absorb large amounts of water, swelling hundreds of times their dry polymer

B. Arsuffi, T. Magrini, C. Daraio
Division of Engineering and Applied Science
California Institute of Technology
Pasadena, CA 91125, USA
E-mail: t.magrini@tue.nl; daraio@caltech.edu

B. Arsuffi, G. Siqueira, G. Nyström
Empa
Swiss Federal Laboratories for Materials Science and Technology
Cellulose and Wood Materials Laboratory
Dübendorf 8600, Switzerland
E-mail: gilberto.siqueira@empa.ch

B. Arsuffi, S. Titotto
Center of Engineering
Modelling and Applied Social Sciences
Federal University of ABC
Santo André, SP 09210-580, Brazil
E-mail: silvia.titotto@ufabc.edu.br

T. Magrini
Department of Mechanical Engineering
Eindhoven University of Technology
Eindhoven 5600 MB, The Netherlands

The ORCID identification number(s) for the author(s) of this article can be found under https://doi.org/10.1002/adfm.202409864

DOI: 10.1002/adfm.202409864

network mass.[21] The most common responsive hydrogels are triggered by heat and are characterized by the presence of hydrophobic groups, such as methyl, ethyl, and propyl.[22] Poly(*N*-isopropylacrylamide) (PNIPAM) is one of the most widely employed thermoresponsive hydrogels, particularly for biomedical applications, since its volume phase transition temperature (VPTT) ≈32 °C is close the body temperature and can be by copolymerization with other co-monomers.[23–25] pH-responsive hydrogels are also extensively utilized as programmable soft materials. In these hydrogels, hydrophilic networks undergo volumetric changes in reaction to variations in the surrounding pH levels.[26] The fundamental components of such hydrogels are polymers with weakly acidic or basic properties, such as poly(acrylic acid) (PAA).[27] In addition, ions play diverse roles in inducing changes in hydrogel swelling, depending on the hydrogel's chemical structure.[28] For instance, ionic interactions have been widely employed to establish physical crosslinking in hydrogels with charged components, such as sodium alginate (SA).[29,30]

Nonetheless, hydrogels commonly exhibit poor mechanical and structural properties, limiting their actuation power and applications.[31,32] Strategies to address this limitation include synthesizing double-network hydrogels,[33] or incorporating reinforcing particles such as nanocelluloses (NC).[34,35] When successfully aligned during hydrogel fabrication, NC reinforcing particles can impart an anisotropic swelling behavior, as well as superior mechanical properties.[36,37] For instance, PNIPAM hydrogels reinforced with 20 wt% CNC presented an increase in stiffness by a factor of 236 compared to the pure matrix.[38] One method to achieve high NC alignment is through direct ink writing (DIW) 3D printing technique.[35,39] In DIW, NC-laden inks are extruded through a nozzle, achieving precise control of the NC particles alignment, critical to achieve the intended in plane actuation, that is necessary for volumetric shape-morphing.[39] The anisotropic shape transformations induced by NC alignment have been used to fabricate programmable actuators within the realm of 4D printing.[40,41] 4D printing consists of prototyping responsive and time-dependent structures through 3D printing technologies.[42] The fourth dimension refers to the capability of the structure to alter its shape, functionality, and/or properties over time in response to specific environmental stimuli during its post-printing lifetime.[43] Programmable hydrogels are among the most used materials for 4D printing,[44] especially within architectures designed to enhance actuation, such as bilayer systems. The swelling mechanism driving bilayer morphism can be achieved through either multi- or mono-material printing. In the multi-material approach, varying water absorption capacities of each hydrogel cause the structure to bend toward the side with the hydrogel exhibiting lower swelling degree.[45,46] Whereas, in the mono-material approach, shape alteration arises from differences in the filament orientation within each layer.[47]

Here, we present, for the first time, nanocellulose-based multi-stimuli-responsive hydrogels, capable of sensing three distinct environmental stimuli and computing logic operations through programmable mechanical actuation. This is achieved by employing five key strategies: i) utilizing stimuli-responsive hydrogels: PNIPAM for temperature and ionic responses, and PAA for pH response; ii) incorporating cellulose nanocrystals (CNCs) and nanofibers (CNFs) as anisotropic reinforcing particles; iii) designing the geometry of filament orientation; iv) fabricating a bilayer system through multi-material 4D printing; and v) tuning the stimuli concentration and combining different stimuli. We develop inks with a high nanocellulose content (15 wt%), investigate their printability, and adjust their processing parameters. Then, we characterize the swelling and shrinking behavior of the hydrogels, as well as their shape-morphing mechanism and mechanical properties in response to multiple stimuli excitations. Finally, we demonstrate the material's programmability both in space and time, exploring Boolean algebra concepts by designing logic gates that leverage the actuation of the bilayer structures. This dual programmability allows the hydrogel composites to be used not only as actuators but also as mechanical sensors.

2. Results and Discussion

2.1. Fabrication of Nanocellulose-Based Multi-Responsive Hydrogels

To fabricate multi-responsive programmable hydrogels, the first step involved preparation of the nanocelluloses. We extracted cellulose nanofibers (CNFs) from wood pulp through TEMPO-oxidation process (**Figure 1a**).[48] CNFs were then used to create 3D printing inks (Figure 1b) through mechanical mixing with other components, including commercially available cellulose nanocrystals (CNCs). The typical ink formulation is detailed in the Experimental Section and summarized here as follows: CNFs (1 wt%), CNCs (14 wt%), deionized water (75.44 wt%), sodium alginate (SA) (1–2 wt%), N-isopropylacrylamide (NIPAM) (8.25 wt%) or acrylic acid (AA) (7.25 wt%), crosslinker (0.06 wt%), and photoinitiator (0.25 wt%) (Tables S1 and S2, Supporting Information). NIPAM and AA serve as the monomers for the smart polymers poly(N-isopropylacrylamide) (PNIPAM) and poly(acrylic acid) (PAA), respectively. PNIPAM is a widely known thermoresponsive hydrogel, characterized by a lower critical solution temperature (LCST) of ≈32 °C. This implies that PNIPAM macromolecules undergo a volume phase transition (VPT) from a well-hydrated state (below 32 °C) to a collapsed state (above 32 °C) (**Figure 2a**).[49] Thus, PNIPAM's volume is drastically altered by small changes in temperature due to the reversible transition of its polymer chains from a hydrophilic to a hydrophobic state at the LCST.[50] Additionally, salt solutions exceeding critical concentrations can also induce an analogous phase transition in PNIPAM. This is because the presence of anions in the surrounding media acts on reducing the LCST. Consequently, its swelling degree demonstrates a reversible decrease with an increase in ionic concentration.[51] In contrast to what is observed in PNIPAM-based hydrogels, the swelling behavior of PAA-based hydrogels is primarily influenced by the surrounding pH (Figure 2a). When the pH exceeds the pKa of 4.3, PAA-based hydrogels undergo swelling and they expand in volume. Conversely, when the pH falls below the pKa, the PAA-based hydrogel undergoes shrinking and decreases in volume.[52] As the PNIPAM- or PAA-hydrogel networks provide stimuli responsiveness, the secondary SA-based network adds rigidity and stiffness to our NC-reinforced double-network hydrogel system, drastically enhancing its structural properties (Figure S5, Supporting Information).[33,44]

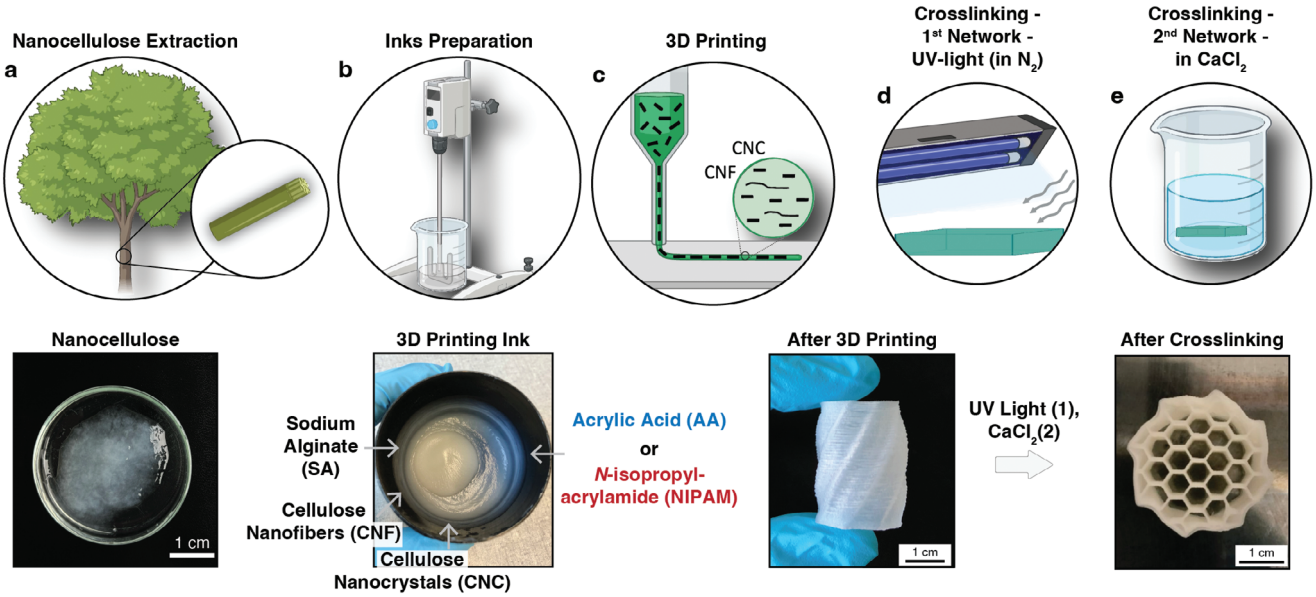

Figure 1. Fabrication process overview of multi-stimuli-responsive nanocellulose-based hydrogels: a) Extraction of CNF from wood pulp. b) Preparation of inks by mixing. c) 3D printing via DIW. d) Photopolymerization of the PNIPAM- or the PAA-based networks. e) Ionic crosslinking of the SA network in $CaCl_2$.

The production of homogeneous inks for DIW with a high NC solid loading is non-trivial, yet it is key for high quality manufacturing, thus requiring the mastering of nanoparticles dispersion in aqueous or non-polar solvents.[35,53] Here, we achieved uniform dispersion of the NC particles in the inks through high-speed mechanical mixing. The homogeneity of the resulting inks was then confirmed using optical microscopy under cross-polarized light (Section S2 and Figure S2, Supporting Information). Moreover, previous works that targeted similar hydrogel-based systems, have demonstrated that rheological properties such as shear-thinning behavior, fast elastic recovery, well-defined yield stress (in the order of 100 Pa), and elastic modulus higher than a few kPa are key parameters that ensure high shape fidelity during the DIW process.[35,38,39] In this work, these properties were achieved by incorporating CNCs (14 wt%) and CNFs (1 wt%) into the inks, which were then evaluated using steady-shear and oscillatory measurements (Section S3 and Figure S3, Supporting Information). Shear thinning was promoted by the alignment of the nanocellulose particles during extrusion (Figure 1c).[39] Yet, the flow-induced orientation of CNCs and CNFs occurs only if the applied stress during printing surpasses the ink's yield stress (i.e., the differential-flow regime).[35] The shear thinning behavior of the inks (Section S3, Supporting Information) allowed for the printing of intricate structures with precise geometry control, such as the 3.5 cm high twisted octagon vase with a honeycomb inner structure, composed of 109 layers (Figure 1c), as well as self-supporting bridges capable of bearing weights 15 times greater than their own (Section S4 and Figure S4, Supporting Information). These examples demonstrate the fabrication versatility of the developed inks. The primary goal of this work, however, was to leverage 3D printing as a processing tool to control the alignment of cellulose nanoparticles (CNCs and CNFs) and to ensure the controllability, repeatability, and reproducibility of the bilayer logic operations with a straightforward readout. After 3D printing, high shape stability was achieved through a dual-step crosslinking process. Photopolymerization was employed to crosslink either the PNIPAM- or the PAA-based networks (Figure 1d), while ionic crosslinking with Ca^{2+} was applied to the SA network (Figure 1c). Both crosslinking processes were confirmed through FTIR analysis and shape-stability experiments (Section S5, Supporting Information).

2.2. Physical Properties of the Composites: Swelling and Shrinking Behavior, Shape-Change, and Stiffness

The swelling capacity of the hydrogel composites was quantified through water absorption tests using fully dried 3D printed samples. Both PNIPAM/SA/NC and PAA/SA/NC hydrogels exhibit similar swelling kinetics, with a rapid growth in water uptake in the first 8 h, followed by a prolonged stabilization, indicating a quick water absorption response due to the higher osmotic pressure between the dry hydrogels and water (Figure 2b). However, because PAA is a superabsorbent material, due to the deprotonation of the carboxylic acid groups of its polymer chain,[52] PAA/SA/NC hydrogel shows much higher values of water absorption than PNIPAM/SA/NC hydrogel. While the PNIPAM/SA/NC hydrogel exhibits over 735% water absorption compared to its dry weight after 5 days of swelling, the PAA/SA/NC hydrogel presents more than three times higher water absorption (2499%) for the same period (Figure 2b). The equilibrium moisture content is achieved after 4 days, when the osmotic pressure balances the retractile forces exerted by the stretching polymer chains.[54] For both PNIPAM/SA/NC and PAA/SA/NC hydrogels, the swelling capacity can be adjusted by controlling the crosslinking density of the SA network. Increasing the $CaCl_2$ concentration, during crosslinking, reduces the hydrogels water

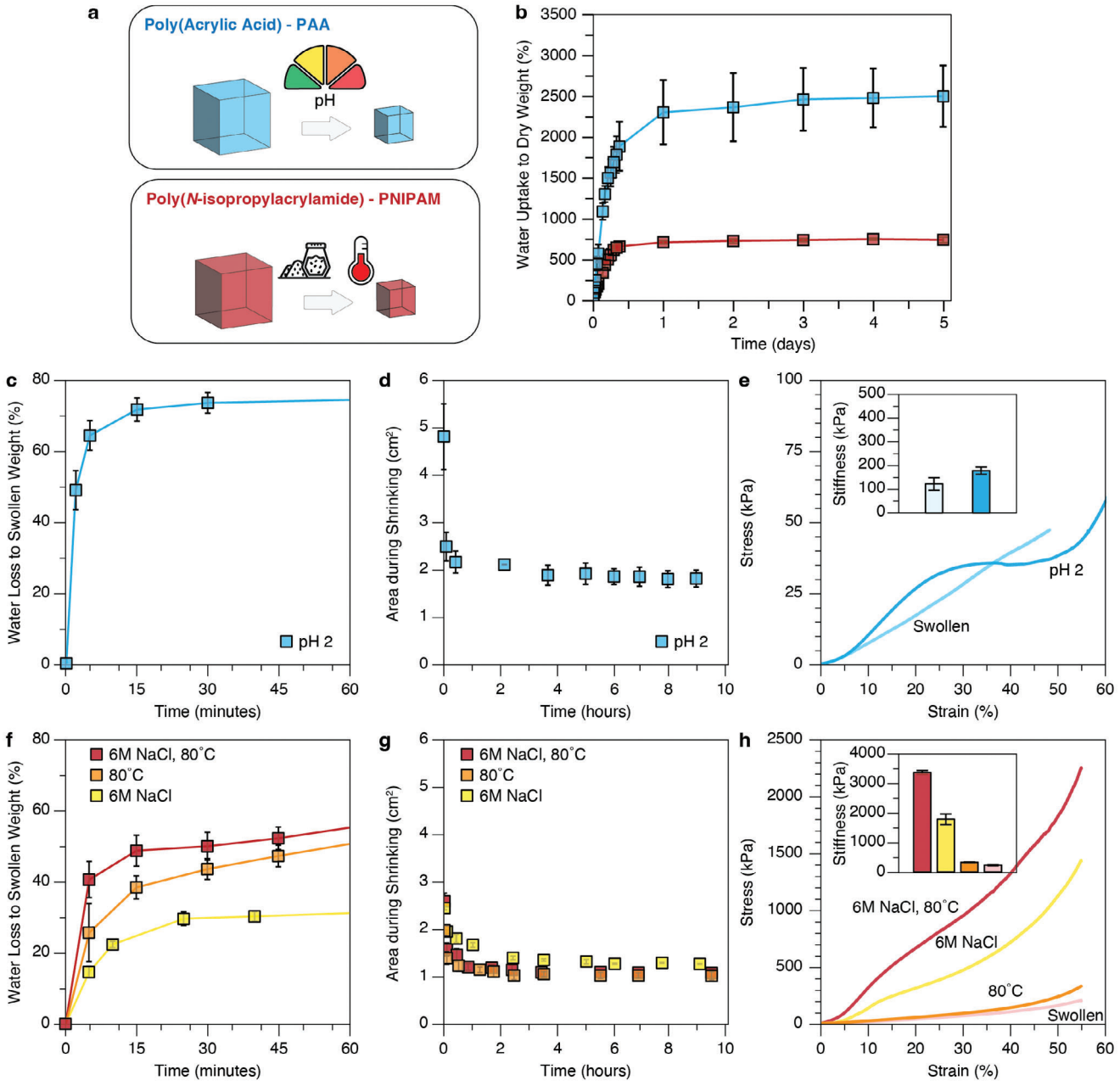

Figure 2. Physical properties of responsive hydrogels. a) Responsivity of PAA- and PNIPAM-based hydrogels to external stimuli. b) Swelling behavior of PNIPAM/SA/NC and PAA/SA/NC hydrogels. c) Shrinking behavior of PAA/SA/NC hydrogel in response to pH. d) Shape-change during shrinking of PAA/SA/NC hydrogel. e) Comparison of average stress versus strain curves and stiffness for PAA/SA/NC hydrogel in its swollen and shrunk states. f) Shrinking behavior of PNIPAM/SA/NC hydrogel in response to temperature and/or salt concentration. g) Shape-change during shrinking of PNIPAM/SA/NC hydrogel. h) Comparison of average stress versus strain curves and stiffness of PNIPAM/SA/NC hydrogel in its swollen and shrunk states. Error bars show standard deviation ($n = 3$).

uptake. For example, the swelling capacity of PNIPAM/SA/NC hydrogel is reduced by a factor of 2.7 when crosslinked with 5 wt% $CaCl_2$, and PAA/SA/NC hydrogel not crosslinked with $CaCl_2$ has a water uptake 12.8 times higher than when crosslinked with 5 wt% $CaCl_2$ (Figure S7, Supporting Information). Higher $CaCl_2$ concentrations create a more extensively crosslinked SA network, restricting hydrogel expansion during swelling and increasing stiffness. Indeed, samples crosslinked with 5 wt% $CaCl_2$ exhibit a Young's modulus over 25 and 149 times higher than samples without ionic crosslinking for PNIPAM/SA/NC and PAA/SA/NC hydrogels, respectively (Figure S8, Supporting Information). This effect is intensified in PAA/SA/NC hydrogels due to their higher SA content compared to PNIPAM/SA/NC hydrogels.

As PNIPAM and PAA are stimuli-responsive hydrogels, the shrinking behavior of the composites upon exposure to

environmental stimuli was studied using fully swollen 3D printed samples. When submerged in acidic solutions with a pH below PAA's pKa (4.3), the PAA/SA/NC hydrogel rapidly shrinks, reaching nearly maximal shrinkage in less than 30 min (Figure 2c). The shrinking rate of the PAA/SA/NC hydrogel increases as the pH level decreases (Section S6 and Figure S9, Supporting Information). For instance, after 1 h in a solution with a pH of 2, the PAA/SA/NC hydrogel shows a water loss of 75% compared to its swollen state (Figure 2c). PNIPAM, in contrast, shrinks in response to temperatures above its LCST (32 °C).[49] The shrinking degree of the PNIPAM/SA/NC hydrogel directly correlates with the heat intensity. At all tested temperatures (40, 60, and 80 °C), the shrinking kinetics of the PNIPAM/SA/NC hydrogel are faster than its swelling kinetics (Section S6 and Figure S9, Supporting Information). Within 1 h at 80 °C, the PNIPAM/SA/NC hydrogel loses 54% of its water compared to its swollen state (Figure 2f). Moreover, the presence of anions in the surrounding media reduces the LCST of PNIPAM.[55] Therefore, the shrinking rate of PNIPAM/SA/NC hydrogel increases with higher salt concentrations in the solution (Section S6 and Figure S9, Supporting Information). For example, after 1 h in a 6 M sodium chloride (NaCl) solution, the hydrogel shows a 32% reduction in water content compared to its swollen state (Figure 2f). Furthermore, when temperature and NaCl stimuli are combined, the shrinking behavior of PNIPAM/SA/NC hydrogel is accelerated. After just 5 min in a 6 M NaCl solution at 80 °C, the hydrogel presents a water loss value exceeding 40%, which increases to over 58% after 1 h (Figure 2f). When the hydrogels shrink, they contract in size (Section S7 and Figure S10, Supporting Information). This shape oscillation can be programmed by adjusting the applied stimulus. A higher stimulus results in greater shrinking and a more pronounced shape change (Section S7 and Figure S12, Supporting Information). For instance, PAA/SA/NC hydrogel undergoes significant contraction in response to pH 2, reducing its top area by over 56% within 2 h (Figure 2d). Similarly, the PNIPAM/SA/NC hydrogel's top area decreases by more than 48% at 80 °C and 43% in a 6 M NaCl solution after 2 h. This contraction intensifies to 56% when the hydrogel is simultaneously exposed to both stimuli (Figure 2g).

The mechanical properties of the composites were assessed through compression tests on fully swollen 3D printed samples. As expected, the reinforcement with nanocellulose particles (both CNC and CNF) positively impacted the stiffness of the composites. The PNIPAM/SA/NC hydrogel has a Young's modulus of 252.94 kPa, which is 48 times higher than that of the PNIPAM/SA matrix without nanocellulose (Section S8 and Figure S13, Supporting Information). Moreover, when the smart hydrogels are exposed to external stimuli, they expel water and experience an increase in polymer chain entanglement, leading to an increase in stiffness.[22] In resonance with the shrinking behavior, the stiffness of the composites can be controlled by modulating the pH, temperature and salt concentration (Section S9 and Figure S14, Supporting Information). For instance, the PNIPAM/SA/NC hydrogel subjected to 80 °C for 24 h shows a modulus 42% higher (323.54 kPa) than that of the swollen hydrogel at 21 °C (Figure 2h). This increase in stiffness is even more pronounced for samples immersed in a NaCl solution. The hydrogel previously immersed in 6 M NaCl exhibits a Young's modulus of 1782.69 kPa, nearly eight times higher than that of the hydrogel not exposed to NaCl (Figure 2h). However, the substantial increase in stiffness at high NaCl concentrations might also be influenced by salt aggregation within the printed structures, in addition to water loss. When both temperature (80 °C) and NaCl (6 M) stimuli are combined, the PNIPAM/SA/NC hydrogel demonstrates a Young's modulus ≈15 times higher (3373.84 kPa) than in its swollen state (Figure 2h). A similar behavior is observed for the PAA/SA/NC hydrogel, which becomes stiffer with a decrease in pH, presenting Young's modulus values of 123.08 kPa at pH 7 and 178.55 kPa at pH 2 (Figure 2e). At pH 2, as the PAA/SA/NC hydrogel is in its shrunk state, its stress–strain curve exhibits a yield plateau indicating plastic deformation. This plateau is absent in the stress–strain curve of the same hydrogel at pH 7 because, at this pH, the hydrogel is swollen and behaves like a soft, rubber-like material with a more flexible polymer chain structure. In addition, the densification of the PAA/SA/NC hydrogel in acid environments is intensified due to the effect of physical entanglement of the TEMPO-CNFs.[56] At lower pH values, the surface charges of the carboxyl groups present in the TEMPO-CNFs may be neutralized, reducing the electrostatic repulsion and increasing the tangling effect.[57] The PAA/SA/NC hydrogel exhibits more significant shrinking in response to pH variations compared to the shrinkage observed in the PNIPAM/SA/NC hydrogel when exposed to temperature and/or NaCl (Figure 2c,f). Despite this, the PAA/SA/NC hydrogel demonstrates a lower increase in Young's modulus during stimulus exposure compared to PNIPAM/SA/NC (Figure 2e,h). This difference can be attributed to the effects of $CaCl_2$ crosslinking. The PAA/SA/NC hydrogel contains twice as much SA as the PNIPAM/SA/NC hydrogel, and no $CaCl_2$ crosslinking was applied during the shrinking tests. Conversely, for the compression tests, the samples were pre-crosslinked with 5 wt% $CaCl_2$ for 24 h.

2.3. Shape-Morphing of Programmable Actuators

2.3.1. Programmability in Space: Anisotropic Shape-Morphing

The elongated shapes of both CNCs and CNFs (**Figure 3**a,b) impart directionality, enabling the fabrication of anisotropic composite structures. The extracted TEMPO-CNFs have a diameter of 5.6 ± 1.7 nm and lengths reaching the micrometer (µm) scale. The CNCs exhibit an average diameter of 6.2 ± 1.4 nm and a length of 119.8 ± 29.3 nm, corresponding to an aspect ratio (L/D) of ≈19. The intense shear and extensional forces applied during DIW induce the alignment of CNCs and CNFs along the direction of the printed filaments.[35,38,39,53,58,59] The alignment of CNCs within printed filaments of the PNIPAM/SA/NC hydrogel was demonstrated using optical microscopy under cross-polarized light (Figure 3c,d). The variations in light and color intensity confirm the alignment of CNCs.[35,58,60] When CNCs are aligned parallel to the polarized filter at 0°, the linearly polarized light passes through the sample without significant interference and is effectively cancelled by the second, oppositely oriented polarizer (analyzer), resulting in a uniform dark appearance (Figure 3c). As the sample is rotated from 0° to 45°, which is the angle of maximum transmittance, different colors emerge and intensify due to increased light scattering by the aligned CNCs (Figure 3d).

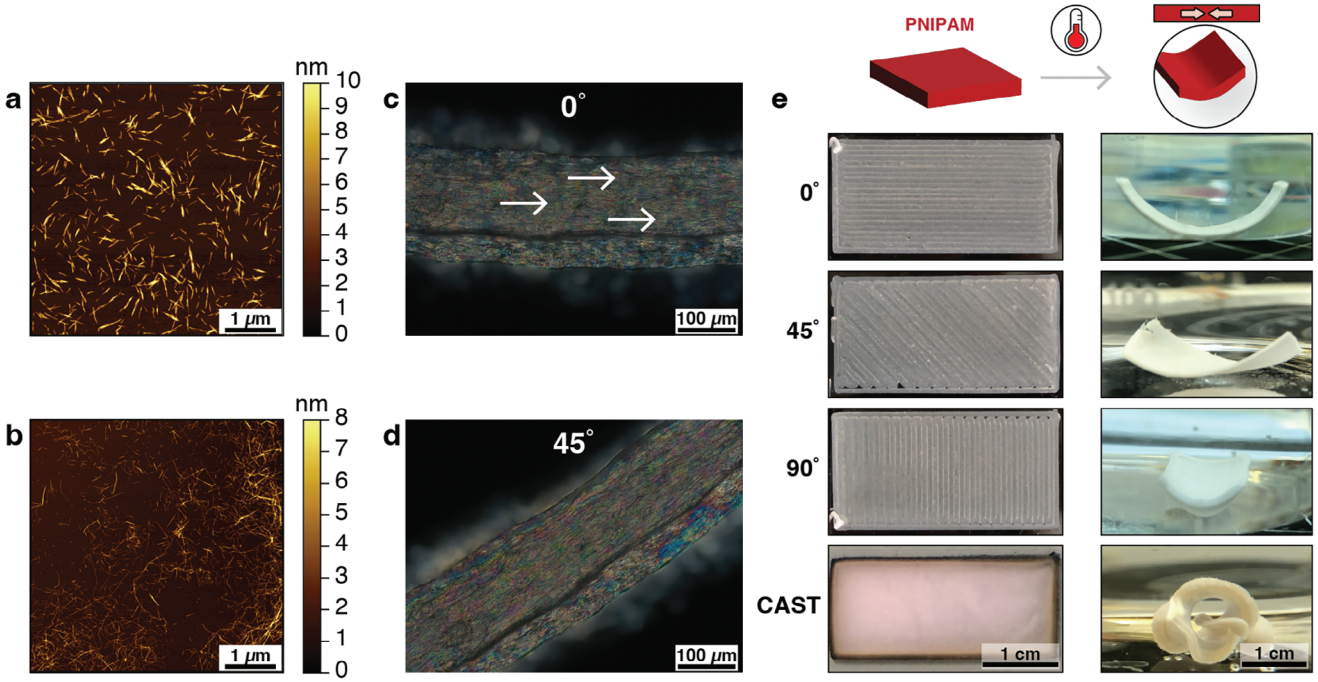

Figure 3. Alignment of cellulose nanoparticles in printed anisotropic actuators. a,b) AFM topographical profiles of (a) CNCs, and (b) extracted TEMPO-CNFs. c,d) Optical microscopy images in cross-polarized light mode (transmission) of PNIPAM/SA/NC hydrogel filaments taken at (c) 0°, and (d) 45°. White arrows indicate the preferential CNC orientation within the hydrogel matrix that corresponds to the printing direction. e) Anisotropic shape-morphing of 3D printed PNIPAM/SA/NC hydrogel actuators with different filament orientations (0°, 45°, and 90°) compared to a cast sample in response to temperature (60 °C) after 5 min.

This alignment facilitates controlled shape-morphing of 3D printed composites, as nanocellulose particles do not expand or contract along their axial direction.[61] Conversely, expansion or contraction primarily occurs perpendicular to the nanocellulose orientation.[38] Additionally, the alignment of cellulose nanoparticles induces different degrees of swelling/shrinking and internal tensions within the hydrogels structures, which can only be reduced through deformations,[44] resulting in highly anisotropic actuation. The anisotropic shape-morphing capability of the PNIPAM/SA/NC hydrogel was investigated using bilayers (30 × 10 × 0.8 mm) printed with varying filament orientations (0°, 45°, and 90°), with both layers sharing the same orientation. As the hydrogel shrinks in response to temperature (60 °C), the initially flat bilayers morph into well-defined 3D structures, following the predetermined filament orientation during 3D printing (Figure 3e). Printing at 0° yields a curved structure, while printing at 90° and 45° produces rolled and twisted architectures, respectively. For comparison, a cast sample composed of the same hydrogel transforms randomly into an uncontrolled shape with no preferred orientation. This contrast supports the conclusion that the shape transformations are guided by the alignment of cellulose nanoparticles (both CNC and CNF) within the printed structures. The actuation behavior of the developed materials is similar to the shape-shifting observed in plant systems, attributed to the reinforcement of cellulose microfibrils in cell walls, as seen in pinecone scales,[62] wheat awns,[63] and orchid tree seedpods.[64] Therefore, precise control over the morphology of the hydrogel structures at the microscale allows for programmable macroscopic shape-morphing akin to the morphological transformations observed in biological systems.

2.3.2. Programmability in Time: Shape-Morphing of Multi-Responsive Bilayers

The ability to control physical properties, such as shrinking capacity, shape, and stiffness, of the stimuli-responsive composites by adjusting their crosslinking density and stimuli intensity enables temporal programmability. This understanding of programmability served as the foundation for designing bilayer actuators with the PNIPAM/SA/NC and PAA/SA/NC hydrogels endowed with controllable shape-morphing. As discussed in the previous section, the geometry of filament orientation significantly influences the shape-morphing of hydrogel sheets. To isolate the impact of this variable on shape alterations of the bilayers, both layers were printed at 0°. Moreover, strong interfacial bonding between the two layers is essential to prevent delamination caused by significant differential dimensional changes during swelling and shrinking.[65] This is especially important in our system since both PNIPAM and PAA contract in volume upon exposure to different stimuli. Furthermore, compatibility between the two hydrogels is crucial, considering factors such as material density, and geometric constraints.[44] Here, the layers were combined through physical adhesion achieved by extruding and depositing the filaments with a 20% overlap of their diameter during the 3D printing process. Additionally, the interfacial bonding was enhanced by the presence of the polymeric network of SA

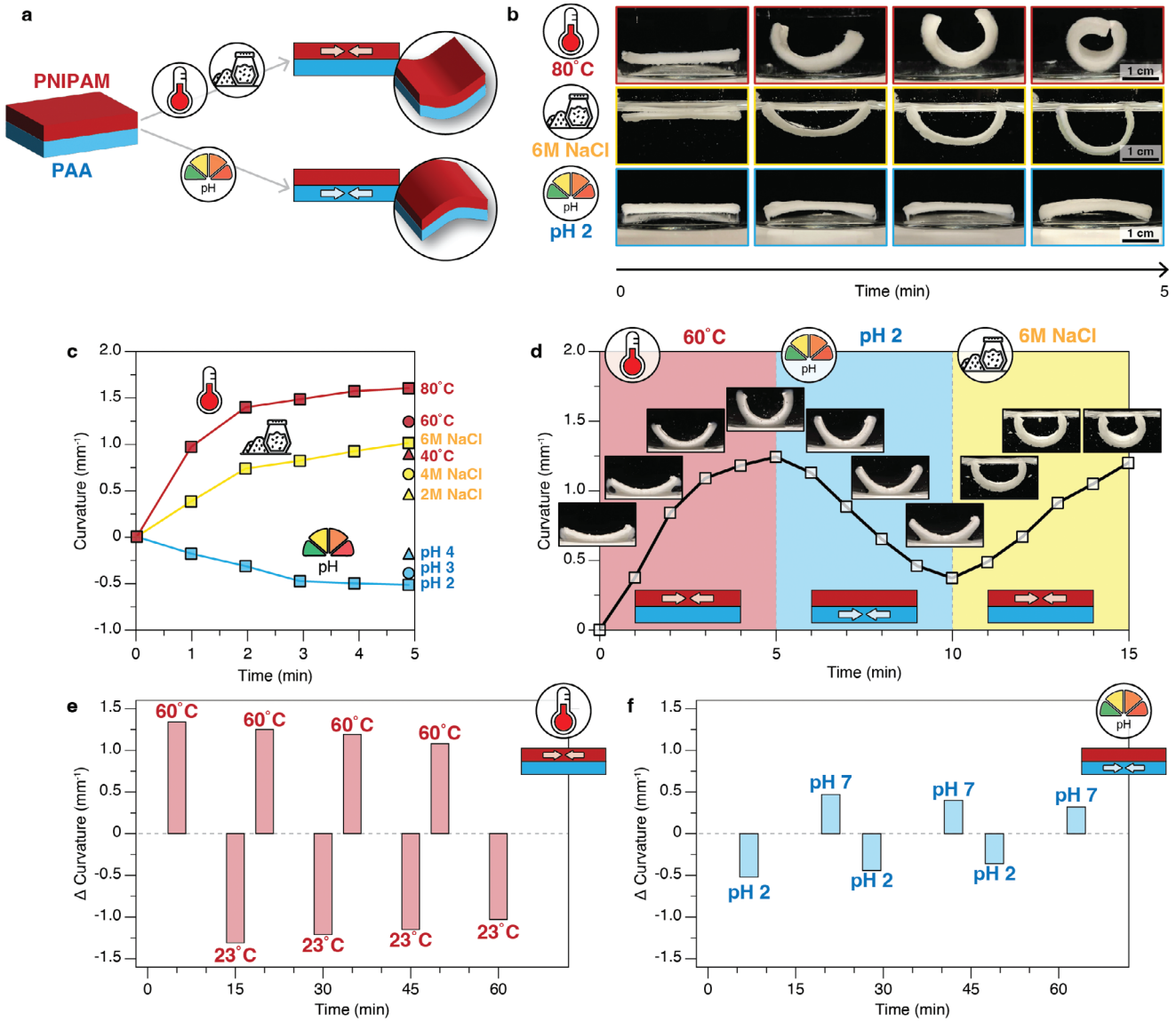

Figure 4. Bilayer system composed of PNIPAM/SA/NC and PAA/SA/NC hydrogels exhibits bending actuation in response to diverse stimulus scenarios. a) Schematics of bilayer actuation resulting from the shrinkage of each layer triggered by external stimuli (temperature, and salt concentration to PNIPAM/SA/NC, and pH to PAA/SA/NC). b) Bidirectional bending of the bilayers observed during a 5-min exposure to temperature (80 °C), NaCl (6 M), and pH (2). c) Alteration in curvature of the bilayers in response to varying stimuli and their intensities. d) Shape-morphing of a bilayer during sequential exposure to stimuli over time: 0 to 5 min at 60 °C, 5 to 10 min at pH 2, and 10 to 15 min at NaCl concentration of 6 M. e) Cyclic actuation of bilayers under temperature variation (23–60 °C). f) Cyclic actuation of bilayers under pH level variation (pH 2 to pH 7).

in both layers and the dual-step crosslinking process involving both materials simultaneously, as they share the same crosslinker and photoinitiator agents. Upon exposure to varying intensities of temperature, pH, and NaCl, the bilayers demonstrated shape-morphing behavior with bidirectional bending, corresponding to the actuation of either the PNIPAM/SA/NC or PAA/SA/NC layer.

In multi-material bilayer systems responsive to external stimuli, shape-morphing is driven by the differential swelling/shrinking capacities of each hydrogel, causing the structure to bend toward the side with the higher shrinking capacity.[45,46] For instance, when exposed to temperatures above 32 °C or high salt concentrations, the top layer of the designed bilayer system, composed of PNIPAM/SA/NC hydrogel, contracts, causing the structure to bend with PNIPAM/SA/NC as the inner layer. Conversely, when immersed in an acidic solution (pH < 4.3), the bottom layer consisting of PAA/SA/NC hydrogel contracts, resulting in bending in the opposite direction, with PAA/SA/NC as the inner layer (**Figure** 4a,b). Thus, depending on the applied stimulus, one layer of the bilayer structure becomes activated and undergoes shrinking, while the other layer remains passive, facilitating bidirectional bending actuation. Moreover, this bending actuation can be programmed by tuning the condition of the surrounding environment. To achieve this, the bilayers were subjected to varying temperatures (20, 40, 60,

80 °C), NaCl concentrations (2, 4, 6 M), and pH levels (2, 3, 4, 7) for a fixed duration of 5 min. As anticipated, the most significant curvature changes were observed under the most intense stimuli: 80 °C, 6 M NaCl, and pH 2 (Figure S15, Supporting Information). Consequently, these conditions were selected for measuring the curvature of the bilayers over time, beginning with fully swollen samples (after being immersed in water at 23 °C for 4 days). For instance, with temperature variations, the bilayer quickly bends toward the PNIPAM/SA/NC side, and the most significant curvature change, from 0.00 to 0.89 mm^{-1}, occurs between 21 and 40 °C, aligning with the LCST of PNIPAM (32 °C).[22] Additionally, when exposed to 80 °C, the average curvature increases to 1.60 mm^{-1} (Figure 4c). Regarding the ionic response of the bilayers, a more pronounced change in curvature, from 0.67 to 1.01 mm^{-1}, is observed between 4 and 6 M NaCl, indicating that a higher salt concentration accelerates the shape-morphing (Figure 4c). However, in acidic solutions, the bilayer bends toward the PAA/SA/NC side, resulting in negative average curvature values. In response to pH, the most significant alteration in curvature, from −0.18 to −0.39 mm^{-1}, happens between pH 4 and pH 3, the closest range to the pKa (4.3) of PAA.[52] When exposed to pH 2, the bilayer reaches a higher average curvature of −0.50 mm^{-1} (Figure 4c).

The shape-morphing results of the bilayers are attributed to the material properties of each hydrogel layer. For example, the bending curvature of the bilayer immersed in 6 M NaCl is lower than that of the bilayer at 80 °C, despite both stimuli inducing similar area changes in the PNIPAM/SA/NC hydrogel (Figure 2g). This difference in curvature may be attributed to osmotic processes occurring in the PAA/SA/NC hydrogel layer and/or salt aggregation within the bilayer's structure at high NaCl concentrations, which could restrict the movement of the PNIPAM/SA/NC layer. Moreover, while the PAA/SA/NC hydrogel alone demonstrates greater responsivity than the PNIPAM/SA/NC hydrogel, evidenced by its higher values of shrinking and area change upon exposure to pH (Figure 2), the bilayer system exhibits the lowest curvature when exposed to pH compared to the other stimuli. This can be attributed to the effect of $CaCl_2$ crosslinking and the difference in stiffness between the two hydrogels. While the shrinking and area-change experiments did not involve $CaCl_2$ crosslinking of the samples, the bilayer structures were crosslinked with 1 wt% of $CaCl_2$ to facilitate strong interfacial bonding between the layers with the SA network. However, it was observed that even this low concentration of $CaCl_2$ significantly reduces (by a factor of 11) the swelling capacity of the PAA/SA/NC hydrogel (Figure S7, Supporting Information). Therefore, the shrinking properties of the PAA/SA/NC hydrogel in the bilayer system are limited due to the $CaCl_2$ crosslinking. Furthermore, the mechanical properties of the PAA/SA/NC hydrogel are comparatively lower than those of the PNIPAM/SA/NC hydrogel. Even in its shrunk state, after 24 h in pH 2, the PAA/SA/NC hydrogel exhibits lower stiffness (178 kPa) than the swollen PNIPAM/SA/NC hydrogel (229 kPa) (Figure 2e,h). Consequently, when the bilayer is immersed in pH 2, the PNIPAM/SA/NC layer is stiffer than the PAA/SA/NC layer. Thus, although the PAA/SA/NC layer contracts due to shrinking, its actuation is constrained by the stiffer PNIPAM/SA/NC layer on top of it.

Understanding the bilayer's mechanism of bidirectional bending with varied curvatures in response to different types and intensities of stimuli enables programmability of the actuator's behavior for complex scenarios, including sequential environmental changes. This capability was explored by subjecting the same bilayer sample to a sequence of three stimuli: first temperature (60 °C), then pH (2), and finally NaCl (6 M), each for 5 min. Initially, under the temperature stimulus, the PNIPAM/SA/NC layer contracts, causing a closing movement. When subsequently immersed in an acidic solution at room temperature (23 °C), the PNIPAM/SA/NC layer undergoes reswelling, while the PAA/SA/NC layer contracts. This differential behavior results in both layers contributing to an opening movement. Finally, in the salt solution, the PAA/SA/NC layer becomes passive again, while the PNIPAM/SA/NC layer reactivates, leading to the restoration of the closing movement. This sequence highlights the bilayer system's ability to function as both a mechanical sensor and actuator, sensing its surrounding environment and undergoing programmed actuation due to its multi-stimuli responsiveness.

However, in the sequential stimuli test (Figure 4d), the actuator did not recover its original flat geometry after being exposed to pH 2 for 5 min. To further investigate this phenomenon, we conducted multiple stimulation tests, varying temperature (23 to 60 °C) and pH levels (pH 2 to pH 7) (Figure 4e,f). In both cases, the reswelling process under neutral conditions (23 °C and pH 7) after exposure to external stimuli was significantly slower than the shrinkage process under triggering conditions. This is attributed to the time required for the polymer chains and cellulose nanoparticles to transition back from their collapsed, shrunken state to their relaxed configuration, along with the time needed for the reformation of hydrogen bonds between the polymer and water molecules.[22] To accommodate for this lag, we designed the cyclic actuation experiments to allow the actuator twice as much time for reswelling as for shrinking. During cyclic actuation, either by temperature variation (from 23 to 60 °C) (Figure 4e), or pH variation (from pH 2 to pH 7) (Figure 4f), a small loss in curvature variation is observed for each cycle, when compared to the previous one. This is a consequence of the hornification effect of the nanocellulose particles, referred to as the agglomeration and irreversible loss of water-holding capacity, and therefore flexibility, experienced when nanocellulose is dried, and then rehydrated.[66] Nevertheless, the bilayers successfully withstood four cycles of actuation in response to temperature (Figure 4e) and three cycles in response to pH (Figure 4f), maintaining similar curvature variations to those observed in the first actuation cycle. This highlights the reversible and cyclic behavior of the actuators, demonstrating their potential as programmable materials for 4D applications.

2.4. Materials Logic

The possibility to modulate the actuation of the developed bilayers by programming which layer is activated or remains passive during exposure to various stimuli scenarios, including combinations of stimuli, enables the programmability of the bilayers to conduct logic operations. In Boolean logic-based systems, binary logic gates operate with two logic levels ("0" and "1") in both

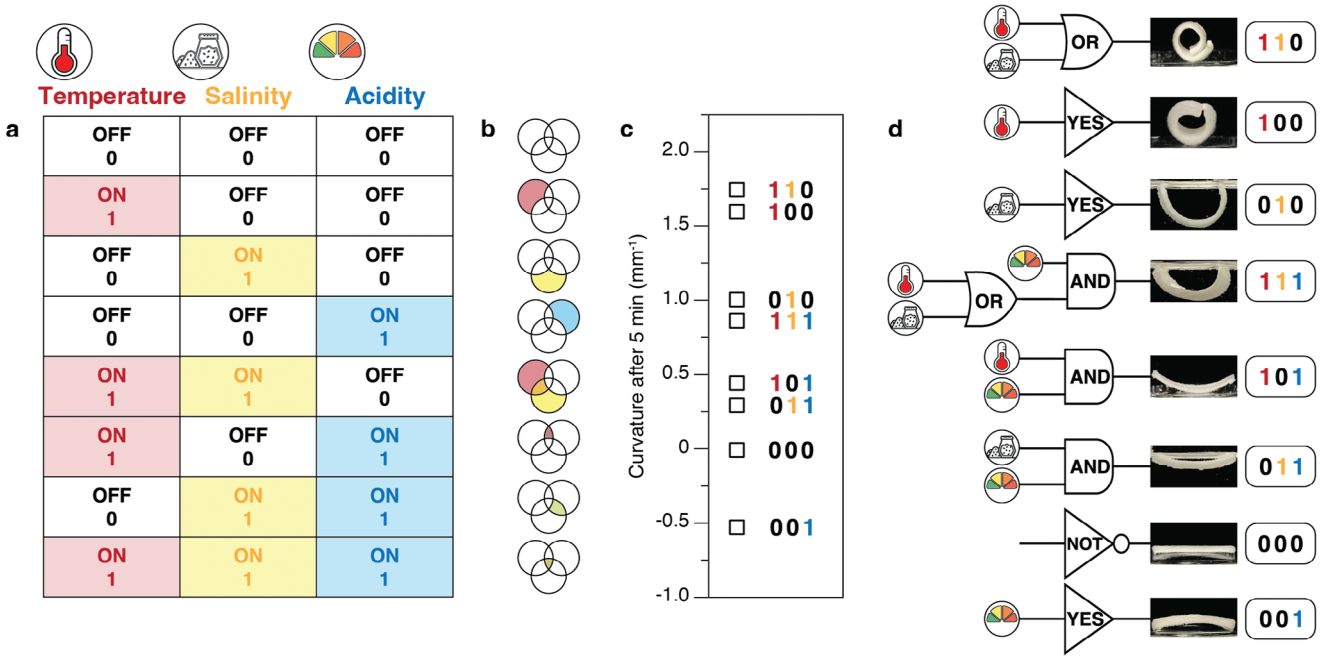

Figure 5. Logic operations performed by bilayer structures in response to combinations of stimuli (temperature, salt concentration, and pH). a) Input table showing binary signals denoted by the presence (ON = 1) or absence (OFF = 0) of stimuli. b) Corresponding Venn diagrams illustrating the presence of stimuli and overlapping regions. c) Bending curvature observed for each of the eight logic operations. d) Representation of logic gates (YES, NOT, OR, AND) with stimuli inputs and resulting shape-morphing outputs.

input and output states.[67] Here, input signals are binary: "0" is assigned when the stimulus is OFF, and "1" when the stimulus is ON. By combining these binary signals corresponding to temperature, NaCl, and pH stimuli, it is possible to generate eight distinct input signals, one for each logic operation, based on the presence and combination of stimuli (**Figure 5**a). Each signal comprises three digits: the first denotes the temperature stimulus, the second denotes NaCl, and the third denotes pH. For instance, the logic operation signal (1 0 1) indicates that temperature and pH are present inputs. Additionally, the logic operations can be represented by Venn diagrams. Each segment of the Venn diagram corresponds to a unique combination of inputs and signifies whether the stimulus is present (colored: red for temperature, yellow for NaCl, and blue for pH) or absent (white) (Figure 5b). To establish the operational logic of the developed system, combinations of stimuli are applied by exposing the bilayers to two or three stimuli simultaneously. While we utilized a binary code for the inputs of the logic operations, the outputs cannot be simply binarized, as they vary based on the resulting shape of the bilayers in response to the applied stimuli combination. Unlike conventional mechanical logic gates that generate discrete digital signals, chemical logic gates rely on responsive materials and exhibit analog signals, dependent on the stimuli.[68]

Hence, the outputs of the logic operations are assessed based on the curvature of the bilayers following the fixed time of 5 min of actuation under each of the eight combinations of stimuli. A different bilayer sample, not previously exposed to any stimulus, was used for each scenario of stimuli combination. The operation (1 1 0) exhibits the highest bilayer curvature value of 1.75 mm^{-1} (Figure 5c). This result arises from the combined effects of the contributing stimuli: temperature (80 °C) and NaCl (6 M), which amplify the shrinking of the PNIPAM/SA/NC layer, leading to a more pronounced bending actuation. Conversely, the (0 0 0) operation, where no stimulus is applied, results in close to zero shape transformation. The second lowest positive curvature value of 0.30 mm^{-1} is observed for the (0 1 1) operation, resulting from the combination of NaCl (6 M) and pH (2), two competing stimuli that induce moderate curvature in both layers (Figure 5c). Similarly, the operation (1 0 1) exhibits a lower curvature actuation of 0.45 mm^{-1}, also attributed to the presence of competing stimuli (temperature and pH), which trigger the actuation of both layers (Figure 5c). In this scenario, the curvature surpasses that of operation (0 1 1) because temperature induces a greater actuation of the PNIPAM/SA/NC layer than NaCl (Figure 4c). Furthermore, for both operations (0 1 1) and (1 0 1), the bending curvature remains positive despite the presence of pH stimulus, which typically induces negative bending, indicating that the actuation force of the PNIPAM/SA/NC layer is stronger than that of the PAA/SA/NC layer. The operation (0 0 1) presents the most negative curvature value of −0.52 mm^{-1}, attributed to the single input of pH (2) activating the PAA/SA/NC layer, resulting in negative bending (Figure 5c). On the other hand, the operations (1 0 0) and (0 1 0) exhibit high curvature values of 1.60 and 1.01 mm^{-1}, respectively, due to the robust actuation of the PNIPAM/SA/NC layer in response to temperature (80 °C) and NaCl (6 M), respectively (Figure 5c). The operation (1 1 1), which combines all the three stimuli (80 °C, 6 M NaCl, pH 2) displays a moderate curvature value of 0.87 mm^{-1} due to the simultaneous shrinking of both PNIPAM/SA/NC and PAA/SA/NC layers (Figure 5c).

Following Boolean logic principles, NOT, YES, OR, and AND gates were constructed, resulting in eight distinct chemical logic

gates, each corresponding to a different stimuli combination (Figure 5d). Stimuli-responsive materials effectively function as YES gates, operating on an ON–OFF principle as a switch mechanism. However, to construct Boolean logic-based systems, materials need to react to multiple inputs to form AND, OR, and other logic gates. Moreover, these materials must react independently, without subsequent or coordinated responses.[68] An OR gate generates an output upon sensing either of two inputs. While numerous multi-stimuli-responsive material systems exist, OR gate necessitates that either stimulus is adequate to induce a response and that they provoke the same response.[68] AND gates demand two inputs to yield a single output. In responsive materials, AND gates enhance specificity, thereby increasing efficiency.[17] Here, a NOT gate is formed by the absence of any stimulus, operation (0 0 0). YES gates are created by exposing the bilayer to one stimulus at a time, either temperature (1 0 0), NaCl (0 1 0), or pH (0 0 1) (Figure 5d). An OR gate is formed by subjecting the bilayer to both temperature and NaCl at the same time (1 1 0), resulting in intense bending actuation, due to the combination of two contribute stimuli (Figure 5d). In contrast, AND gates are based on the interaction of competing stimuli. Two AND gates are created by exposing the bilayer to pH and temperature (1 0 1), or to pH and NaCl (0 1 1), causing both layers to shrink simultaneously (Figure 5d). Additionally, a more intricate logic operation is conducted by combining an OR gate with an AND gate. When the bilayer is exposed to all stimuli at the same time (1 1 1), both layers become active. The temperature and NaCl stimuli contribute to an OR gate, which feeds its output as one of the inputs, along with pH (a competing stimulus), to an AND gate, resulting in moderate bending actuation (Figure 5d). Therefore, the materials logic developed here relies on chemical logic gates yielding mechanical actuation outputs. These analog outputs, derived from the curvature of the bilayers, offer advantages over the digital outputs of conventional logic materials. One benefit lies in sensing subtle nuances in data.[68] Given the reversible behavior of the bilayers (Figure 4e,f), each actuator can be reused as a mechanical sensor, ensuring shape stability and accuracy in logic computation.

3. Conclusion

We have designed and fabricated actuators with embodied logic using responsive hydrogels (PAA and PNIPAM) reinforced with high concentration of nanocellulose (14 wt% CNC and 1 wt% CNF) through 4D printing. By adjusting the stimuli, we determined the physical properties of the multi-responsive composites, including swelling capacity, stiffness, and shape-morphing ability, necessary to characterize their response under different environmental conditions. This enabled both temporal and spatial programmability of the bidirectional bending actuation in bilayer structures triggered by temperature, NaCl, and pH variations. The combination of these stimuli generated various responsiveness scenarios, which we used to demonstrate NOT, YES, OR, and AND logic gates, accomplishing eight different logic operations. The analog outputs (a range of intermediate curvatures) from these operations highlight the potential of the developed material as a mechanical sensor with a simple optical readout. Further exploration of the anisotropic properties provided by the alignment of the nanocellulose particles could enable extra logic operations. Additionally, integrating more degrees of programmability into the materials by tailoring the crosslinking density in different regions of the structure could induce localized properties, further enhancing the versatility of the actuators. Therefore, the reported programmable multi-responsive hydrogels provide a novel approach to designing logic material systems that can be leveraged for autonomous soft robotics, biomedical diagnostic, drug delivery, smart agriculture, and environmental monitoring and remediation.

4. Experimental Section

Materials: For the TEMPO-mediated oxidation: 2,2,6,6-tetramethyl-1-piperidinyloxyl (TEMPO), sodium bromide (NaBr) 99%, and sodium hypochlorite solutions (NaClO) (12–14% chlorine) were purchased from VWR International (Belgium). Sodium hydroxide (NaOH) 99% was acquired from Carl Roth GmbH + Co. KG (Germany). For the preparation of the precursor gels: lyophilized cellulose nanocrystals (CNCs) from acid hydrolysis of eucalyptus pulp were acquired from CelluForce (Canada), and cellulose fibers, derived from bleached wood pulp, were used for the production of cellulose nanofibers (CNFs). The monomers *N*-isopropylacrylamide (NIPAM) 97%, and acrylic acid (AA) 99%, as well as the crosslinking agent *N,N'*-methylenebis(acrylamide) (MBA) 99%, sodium alginate (SA), calcium chloride ($CaCl_2$), sodium chloride (NaCl), and hydrochloric acid (HCl) were acquired from Sigma–Aldrich. The photoinitiator lithium phenyl-2,4,6-trimethylbenzoylposphinate (LAP) 99% was purchased from Apollo Scientific (England).

Fabrication of Cellulose Nanofibers (CNF): Never-dried cellulose fibers were TEMPO oxidized following a well-established protocol from Saito and Isogai,[69] which was extensively described elsewhere.[48] The oxidized cellulose fibers were separated from the solution, by using metal and cotton fabric filters, and were thoroughly washed with distilled water for 5 days, until the conductivity was similar to that of distilled water. The oxidized cellulose fibers were dispersed in deionized water to a concentration of 2 wt% and grounded using a Supermass Colloider (MKZA10- 20 J CE Masuko Sangyo, Japan) to obtain a suspension of cellulose nanofibers (CNFs). The energy applied to the grinding process was 10 kWh per kg of cellulose.

Preparation of Nanocellulose-Based Inks: The dispersion of the cellulose nanoparticles (14 wt% CNC, and 1 wt% CNF) and the other ingredients (75.44 wt% of deionized water, 1.00 wt% of SA, 8.25 wt% of NIPAM, 0.06 wt% of MBA, and 0.25 wt% LAP) (Table S1, Supporting Information) was achieved by mechanical mixing of the inks either using a speedmixer (SpeedMixer DAC 150.1 FVZ) at speeds 1000, 1500, 2000, and 2350 rpm for 1 min each and repeating this program for three times, or using an overhead mechanical stirrer (BDC3030, Caframo) at 1300 rpm for 15 min with a metallic rod and a 4 cm cross-shaped impeller. The same procedure has been adopted for the AA-based ink, with the only alteration being the substitution of NIPAM with AA (7.25 wt%) and an increase in the SA content to 2 wt% (Table S2, Supporting Information). The nanocellulose-based inks were stored in the fridge (4 °C) for one night. Before printing, the gel was filled into plastic syringe cartridges and centrifuged (centrifuge ROTINA-380 Hettich, or 5804 Eppendorf) for 4 min at 3500 rpm to remove air bubbles.

Rheology of Inks: The rheological behavior of the developed inks was characterized using a rotational rheometer (MCR 302, Anton Paar), and using non-crosslinked hydrogels, without the presence of the photoinitiator. Measurements were carried out with a parallel plates geometry, with a diameter of 50 mm and a spacing of 0.5 mm at a constant temperature of 20 °C. The flow viscosity was obtained by varying the rotational shear rate from 0.001 to 1000 s^{-1} with a logarithmic sweep. With the amplitude sweeps, the elastic shear modulus (G') and viscous modulus (G″) were measured using logarithmic oscillatory intervals at a frequency of 1 Hz (deformation variations from 0.01 to 1000%). The apparent yield stress was defined as the shear stress when the storage and loss moduli intersect, i.e., the gel point.

3D Printing: Nanocellulose-based hydrogels were 3D printed using the direct ink writing (DIW) technique with equipment from EnvisionTEC (Bioplotter Manufacturing Series) and 3D Systems (Allevi 2). The hydrogels were loaded into plastic cartridges and extruded through uniform steel nozzles (J.A. Crawford co.) at room temperature (23 °C), utilizing compressed air at pressures ranging from 1.1 to 1.7 bar and speeds between 8.0 and 11.5 mm s^{-1}. The extrusion needles were 25.0 mm long and had a non-tapered geometry with diameters of 0.7 mm for the AA ink and 0.4 mm for the NIPAM ink.

Crosslinking: Following the 3D printing process, the hydrogel structures underwent crosslinking through two sequential steps: 1) photopolymerization of the PNIPAM or PAA network, by using ultraviolet (UV) light irradiation in a nitrogen (N_2) atmosphere to prevent oxygen inhibition of the reaction, the structures were placed within a chamber equipped with UV lamps (50 W power, 365 nm wavelength, Everbeam), positioned 5 cm away from the lamps, for 3 to 10 min, depending on the dimensions and thickness of the printed structure; 2) crosslinking the SA network, by immersing the printed and UV-cured structures in an aqueous solution containing either 1 or 5 wt% calcium chloride ($CaCl_2$) for 24 h, this immersion facilitates ionic crosslinking between the alginate molecules and Ca^{2+} ions.

Fourier Transform InfraRed Spectroscopy (FTIR): InfraRed spectra of dried PNIPAM/SA/NC and PAA/SA/NC hydrogels (i.e., dried at RT for 48 h), as well as of AA, NIPAM, SA, TEMPO-CNF (dried at RT for 24 h), and CNC were recorded in a FTIR spectroscope equipped with a ZnSe attenuated total reflectance (ATR) cell (Tensor 27 IR, Bruker). The FTIR-spectra were recorded from 500 to 4000 cm^{-1} with 32 scans and a resolution of 4 cm^{-1}.

Microstructural Characterization—Atomic Force Microscopy (AFM): AFM topographical profiles were used to assess the morphology of CNCs and TEMPO-CNFs. The AFM measurements were carried out using a Bruker Icon3 AFM using RTESPA-150 tips for tapping in soft tapping mode, with a vibration frequency of 150 kHz. First, the freshly prepared mica was treated with 3-aminopropyl triethoxysilane (APTES) at a concentration of 0.05 wt%. After incubating the mica for 1 min, the excess APTES was rinsed off with Milli-Q water and the mica was dried using compressed air. Next, CNCs and TEMPO-CNFs were diluted with Milli-Q water to a concentration of 0.001 wt%. Subsequently, 100 µL of the diluted CNCs and TEMPO-CNFs were placed on the functionalized mica separately. They were left on the mica for 5 min before excess material was rinsed away with Milli-Q water and dried with compressed air. Measurements of diameters of CNCs and CNFs were based on the vertical cantilever displacement, while length of CNCs were measured by image analysis.[70]

Microstructural Characterization—Scanning Electron Microscopy (SEM): The morphology of TEMPO-CNF was investigated by electron microscopy using an FEI Quanta 650 SEM at a working distance of 10 mm and an accelerating voltage of 5 kV. The TEMPO-CNF solution was diluted with Milli-Q water to a concentration of 0.02 wt%, and a 7 nm platinum layer was sputtered onto the samples as a conductive layer.

Microstructural Characterization—Optical Microscopy (OM): An optical microscope (Zeiss Axioplan, equipped with a digital camera Leica DFC 420) in cross-polarized light mode (transmission) was used to observe the morphology of the homogenized inks and to assess the alignment of CNCs in the printed filaments. For the filaments, analysis was conducted using a multi-focus technique, with samples rotated from 0° to 45° relative to the polarizer.

Microstructural Characterization—Swelling Characterization: Time-dependent swelling tests were conducted to quantify the maximal swelling capability of the hydrogels. Printed cubic samples (1 × 1 × 1 cm) with 100% infill and non-crosslinked with $CaCl_2$ were used. For the swelling tests, initially, the samples were completely dried in an oven at 60 °C for 4 h. Then, they were weighed and submerged in distilled water at room temperature for varying durations, ranging from 5 min to 5 days. Following each specified period, the samples were removed from the water, placed on a paper towel to remove excess water from the surface, and then weighed again in their swollen state. A minimum of three samples of the same material were measured for each swelling period. The swelling percentage, also known as equilibrium moisture content (EMC), of the material from fully dried hydrogel samples was calculated Equation (1).

$$Swelling\ (\%) = \frac{W_s - W_d}{W_d} \times 100 \quad (1)$$

Where *Ws* is the weight of the swollen sample, and *Wd* is the weight of the dry sample.

Microstructural Characterization—Shrinking Characterization: To determine the shrinking percentage of the hydrogels in response to different stimuli, fully swollen PNIPAM/SA/NC hydrogel samples (after 4 days immersed in room temperature DI water) were submerged in DI water at 40, 60, and 80 °C, as well as in solutions with varying NaCl concentrations (2, 4, 6 M) for durations ranging from 2 min to 3 days. Similarly, fully swollen PAA/SA/NC hydrogels were immersed in acid solutions with pH 2, 3, and 4, also for various controlled periods of time. At least three samples of the same material and stimuli conditions were measured for each shrinking period. The shrinking capacity of the hydrogels was assessed in terms of the loss of water from the samples compared to their swollen weight Equation (2).

$$Shrinking\ (\%) = \frac{W_s - W_c}{W_s} \times 100 \quad (2)$$

Where *Ws* is the weight of the swollen sample, and *Wc* is the weight of the shrunk sample.

Area Change Characterization: In order to investigate the change in size of the PNIPAM/SA/NC and PAA/SA/NC hydrogels during swelling and shrinking tests, top view pictures of each sample were taken for 10 h of experiment. The top view area of the cubic samples was measured using the image analysis software ImageJ and the percentage of area change after 24 h of swelling was calculated Equation (3).

$$Area\ change\ in\ swelling\ (\%) = \frac{A - A_0}{A_0} \times 100 \quad (3)$$

Where *A* is the area of the swollen sample, and A_0 is the area of the dried sample.

Similarly, it was calculated the percentage of area change after 24 h of shrinking Equation (4).

$$Area\ change\ in\ shrinking\ (\%) = \frac{A_0 - A}{A_0} \times 100 \quad (4)$$

Where A_0 is the area of the fully swollen sample, and *A* is the area of the shrunk sample.

Mechanical Characterization: To assess the mechanical properties of the hydrogels, cubic samples (1 × 1 × 1 cm) with 100% infill were printed and subjected to compression testing using a universal testing machine (ElectroPuls E3000, INSTRON) equipped with a 250 N load cell or (Zwick Roell – Z005 Universal Testing System) with a 100 N load cell, operating at a rate of 1 mm min^{-1}. Additionally, samples of the hydrogel matrices without nanocellulose reinforcement were manually cast and cut, as printing these solutions was not feasible due to their low viscosity. Prior to compression testing, samples were immersed in a solution of 5 wt% of $CaCl_2$ for 24 h of crosslinking, and then they were placed in DI water for 4 days until they reached their fully swollen state. Paper towels were used to gently remove excess water from the surfaces of the specimens. For the stimuli responsiveness tests, the samples were exposed to variations in temperature, NaCl concentration, and pH for 24 h prior to compression testing. At least three specimens were examined for each type of hydrogel and each stimulus parameter. The stiffness of the materials was determined by the elastic modulus, or Young's modulus, which was calculated by analyzing the slope of the elastic region at the initial stage of the stress versus strain curve.

Bilayer Structure Fabrication: A layer of PNIPAM/SA/NC hydrogel was printed on top of a layer of PAA/SA/NC hydrogel, having both layers 100%

infill and filament orientation of 0°. The filaments were extruded and deposited layer-by-layer with a 20% overlap of their diameter, ensuring robust physical adhesion between the layers. This overlap was controlled by setting the filament diameter to 80% of the needle diameter during printing. The multi-material-bilayers were crosslinked with 1 wt% $CaCl_2$ solution for 24 h.

Shape-Morphing Characterization: The bilayer structures were submerged in various solutions to expose them to different intensities of stimuli: temperature (40, 60, 80 °C), NaCl concentration (2, 4, 6 M), and pH levels (2, 3, 4); individually as well as in combinations, for a duration of 5 min each. Front-view photos of the samples were captured, and the average curvature of each sample was calculated using the Kappa plugin[71] in the image processing software Fiji (ImageJ).[70]

Supporting Information

Supporting Information is available from the Wiley Online Library or from the author.

Acknowledgements

The authors thank C. Fox for helping with the operation of the universal testing machine, E. Boschi for the AFM analysis, A. Huch for the SEM and OM imaging, and M. Champeau for helpful discussions. S.T. and B.A. acknowledge funding from the São Paulo Research Foundation (FAPESP) (Grant Nos. #2021/00380-4, #2021/10037-5, #2022/10706-7, and #2023/04970-6). G.S., G.N., and B.A. acknowledge funding from the Schweizerische Eidgenossenschaft, State Secretariat for Education, Research and Innovation (SERI), and from the Circular Bio-based Europe Joint Undertaking (CBE-JU) (Project Bio-LUSH, Grant No. 101112476 to EP). T.M. acknowledges support from the Swiss National Science Foundation (P500PT_203197/1). C.D. acknowledges support from the US National Science Foundation (Grant No. 2308575).

Conflict of Interest

The authors declare no conflict of interest.

Author Contributions

B.A., G.S., T.M., G.N., S.T., and C.D. designed the study. B.A. conducted the experiments, processed the data, and wrote the manuscript with input from all coauthors. All authors reviewed and commented on the manuscript.

Data Availability Statement

The data that support the findings of this study are available from the corresponding author upon reasonable request.

Keywords

4D printing, materials logic, multi-stimuli-responsiveness, nanocellulose hydrogels, programmable materials

Received: June 6, 2024
Revised: September 10, 2024
Published online:

[1] Y. Dong, A. N. Ramey-Ward, K. Salaita, *Adv. Mater.* **2021**, *33*, 2006600.
[2] X. Fan, J. Y. Chung, Y. X. Lim, Z. Li, X. J. Loh, *ACS Appl. Mater. Interfaces* **2016**, *8*, 33351.
[3] P. Lavrador, M. R. Esteves, V. M. Gaspar, J. F. Mano, *Adv. Funct. Mater.* **2021**, *31*, 2005941.
[4] F. G. Woodhouse, J. Dunkel, *Nat. Commun.* **2017**, *8*, 15169.
[5] B. Mazzolai, A. Mondini, E. Del Dottore, L. Margheri, F. Carpi, K. Suzumori, M. Cianchetti, T. Speck, S. K. Smoukov, I. Burgert, T. Keplinger, G. D. F. Siqueira, F. Vanneste, O. Goury, C. Duriez, T. Nanayakkara, B. Vanderborght, J. Brancart, S. Terryn, S. I. Rich, R. Liu, K. Fukuda, T. Someya, M. Calisti, C. Laschi, W. Sun, G. Wang, L. Wen, R. Baines, S. K. Patiballa, et al., *Multifunct. Mater.* **2022**, *5*, 032001.
[6] X. Xia, C. M. Spadaccini, J. R. Greer, *Nat. Rev. Mater.* **2022**, *7*, 683.
[7] P. Jiao, J. Mueller, J. R. Raney, X. (Rayne) Zheng, A. H. Alavi, *Nat. Commun.* **2023**, *14*, 6004.
[8] S. B. Choi, *Front. Mater.* **2014**, *1*, 11.
[9] C. El Helou, P. R. Buskohl, C. E. Tabor, R. L. Harne, *Nat. Commun.* **2021**, *12*, 1633.
[10] H. Yasuda, P. R. Buskohl, A. Gillman, T. D. Murphey, S. Stepney, R. A. Vaia, J. R. Raney, *Nature* **2021**, *598*, 39.
[11] A. Pal, M. Sitti, *Proc. Natl. Acad. Sci. USA* **2023**, *120*, 15.
[12] Y. Song, R. M. Panas, S. Chizari, L. A. Shaw, J. A. Jackson, J. B. Hopkins, A. J. Pascall, *Nat. Commun.* **2019**, *10*, 882.
[13] Y. Jiang, L. M. Korpas, J. R. Raney, *Nat. Commun.* **2019**, *10*, 128.
[14] B. Treml, A. Gillman, P. Buskohl, R. Vaia, *Proc. Natl. Acad. Sci. USA* **2018**, *115*, 6916.
[15] T. Mei, Z. Meng, K. Zhao, C. Q. Chen, *Nat. Commun.* **2021**, *12*
[16] H. Komatsu, S. Matsumoto, S. ichi Tamaru, K. Kaneko, M. Ikeda, I. Hamachi, *J. Am. Chem. Soc.* **2009**, *131*, 5580.
[17] B. A. Badeau, M. P. Comerford, C. K. Arakawa, J. A. Shadish, C. A. Deforest, *Nat. Chem.* **2018**, *10*, 251.
[18] X. Zhang, S. Soh, *Adv. Mater.* **2017**, *29*, 1606483.
[19] A. S. Hoffman, *Adv. Drug Delivery Rev.* **2012**, *64*, 18.
[20] L. Yahia, *J. Biomed. Sci.* **2015**, *4*, 1.
[21] E. M. Ahmed, *J. Adv. Res.* **2015**, *6*, 105.
[22] L. Tang, L. Wang, X. Yang, Y. Feng, Y. Li, W. Feng, *Prog. Mater. Sci.* **2021**, *115*, 100702.
[23] M. J. Ansari, R. R. Rajendran, S. Mohanto, U. Agarwal, K. Panda, K. Dhotre, R. Manne, A. Deepak, A. Zafar, M. Yasir, S. Pramanik, *Gels* **2022**, *8*, 70454.
[24] X. Xu, Y. Liu, W. Fu, M. Yao, Z. Ding, J. Xuan, D. Li, S. Wang, Y. Xia, M. Cao, *Polymers* **2020**, *12*, 580.
[25] Y. Guan, Y. Zhang, *Soft Matter* **2011**, *7*, 6375.
[26] S. Dutta, D. Cohn, *J. Mater. Chem. B* **2017**, *5*, 9514.
[27] L. S. Lim, N. A. Rosli, I. Ahmad, A. Mat Lazim, M. C. I. Mohd Amin, *Nanomaterials* **2017**, *7*, 399.
[28] P. Cao, L. Tao, J. Gong, T. Wang, Q. Wang, J. Ju, Y. Zhang, *ACS Appl. Polym. Mater* **2021**, *3*, 6167.
[29] J. Lai, X. Ye, J. Liu, C. Wang, J. Li, X. Wang, M. Ma, M. Wang, *Mater. Des.* **2021**, *205*, 109699.
[30] A. Kirillova, R. Maxson, G. Stoychev, C. T. Gomillion, L. Ionov, *Adv. Mater.* **2017**, *29*, 1703443.
[31] M. L. Oyen, *Int. Mater. Rev.* **2014**, *59*, 44.
[32] L. E. Beckett, J. T. Lewis, T. K. Tonge, L. S. T. J. Korley, *ACS Biomater. Sci. Eng.* **2020**, *6*, 5453.
[33] S. E. Bakarich, R. Gorkin, M. In Het Panhuis, G. M. Spinks, *Macromol. Rapid Commun.* **2015**, *36*, 1211.
[34] K. J. De France, E. D. Cranston, T. Hoare, *ACS Appl. Polym. Mater* **2020**, *2*, 1016.
[35] G. Siqueira, D. Kokkinis, R. Libanori, M. K. Hausmann, A. S. Gladman, A. Neels, P. Tingaut, T. Zimmermann, J. A. Lewis, A. R. Studart, *Adv. Funct. Mater.* **2017**, *27*, 1604619.
[36] N. Peng, D. Huang, C. Gong, Y. Wang, J. Zhou, C. Chang, *ACS Nano* **2020**, *14*, 16169.

[37] L. Y. Ee, S. F. Yau Li, *Nanoscale Adv.* **2021**, *3*, 1167.
[38] O. Fourmann, M. K. Hausmann, A. Neels, M. Schubert, G. Nyström, T. Zimmermann, G. Siqueira, *Carbohydr. Polym.* **2021**, *259*, 117716.
[39] M. K. Hausmann, P. A. Rühs, G. Siqueira, J. Läuger, R. Libanori, T. Zimmermann, A. R. Studart, *ACS Nano* **2018**, *12*, 6926.
[40] A. Sydney Gladman, E. A. Matsumoto, R. G. Nuzzo, L. Mahadevan, J. A. Lewis, *Nat. Mater.* **2016**, *15*, 413.
[41] C. Gauss, K. L. Pickering, L. P. Muthe, *Compos. Part C: Open Access* **2021**, *4*, 100113.
[42] S. Tibbits, *Archit. Des.* **2014**, *84*, 116.
[43] J. Choi, O. C. Kwon, W. Jo, H. J. Lee, M. W. Moon, *3D Print. Addit. Manuf.* **2015**, *2*, 159.
[44] M. Champeau, D. A. Heinze, T. N. Viana, E. R. de Souza, A. C. Chinellato, S. Titotto, *Adv. Funct. Mater.* **2020**, *30*, 1910606.
[45] W. Liu, L. Geng, J. Wu, A. Huang, X. Peng, *Compos. Sci. Technol.* **2022**, *225*, 109494.
[46] Y. C. Huang, Q. P. Cheng, U. S. Jeng, S. H. Hsu, *ACS Appl. Mater. Interfaces* **2023**, *15*, 5798.
[47] M. C. Mulakkal, R. S. Trask, V. P. Ting, A. M. Seddon, *Mater. Des.* **2018**, *160*, 108.
[48] R. Weishaupt, G. Siqueira, M. Schubert, P. Tingaut, K. Maniura-Weber, T. Zimmermann, L. Thöny-Meyer, G. Faccio, J. Ihssen, *Biomacromolecules* **2015**, *16*, 3640.
[49] K. Matsumoto, N. Sakikawa, T. Miyata, *Nat. Commun.* **2018**, *9*, 2315.
[50] Y. Chen, W. Xu, W. Liu, G. Zeng, *J. Mater. Res.* **2015**, *30*, 1797.
[51] X. Yan, Y. Chu, B. Liu, G. Ru, Y. Di, J. Feng, *Phys. Chem. Chem. Phys.* **2020**, *22*, 12644.
[52] T. Swift, L. Swanson, M. Geoghegan, S. Rimmer, *Soft Matter* **2016**, *12*, 2542.
[53] M. K. Hausmann, G. Siqueira, R. Libanori, D. Kokkinis, A. Neels, T. Zimmermann, A. R. Studart, *Adv. Funct. Mater.* **2020**, *30*, 1904127.
[54] D. Buenger, F. Topuz, J. Groll, *Prog. Polym. Sci.* **2012**, *37*, 1678.
[55] T. Gwan Park, A. S. Hoffman, *Macromolecules* **1993**, *26*, 5045.
[56] M. A. S. A. Samir, F. Alloin, M. Paillet, A. Dufresne, *Macromolecules* **2004**, *37*, 4313.
[57] J. Y. Park, C. W. Park, S. Y. Han, G. J. Kwon, N. H. Kim, S. H. Lee, *Polymers* **2019**, *11*, 414.
[58] L. A. E. Müller, A. Demongeot, J. Vaucher, Y. Leterrier, J. Avaro, M. Liebi, A. Neels, I. Burgert, T. Zimmermann, G. Nyström, G. Siqueira, *ACS Appl. Mater. Interfaces* **2022**, *14*, 16703.
[59] Y. Nagel, D. Sivaraman, A. Neels, T. Zimmermann, S. Zhao, G. Siqueira, G. Nyström, *Small Struct.* **2023**, *4*
[60] E. D. Cranston, D. G. Gray, *Colloids Surf A Physicochem. Eng. Asp.* **2008**, *325*, 44.
[61] I. Burgert, P. Fratzl, *Philos. Trans. R. Soc., A* **2009**, *367*, 1541.
[62] D. Correa, S. Poppinga, M. D. Mylo, A. S. Westermeier, B. Bruchmann, A. Menges, T. Speck, *Philos. Trans. R. Soc., A* **2020**, *378*, 2167.
[63] P. Fratzl, R. Elbaum, I. Burgert, *Faraday Discuss.* **2008**, *139*, 275.
[64] R. M. Erb, J. S. Sander, R. Grisch, A. R. Studart, *Nat. Commun.* **2013**, *4*, 1712.
[65] J. W. Boley, W. M. Van Rees, C. Lissandrello, M. N. Horenstein, R. L. Truby, A. Kotikian, J. A. Lewis, L. Mahadevan, *Proc. Natl. Acad. Sci. USA* **2019**, *116*, 20856.
[66] C. Eyholzer, N. Bordeanu, F. Lopez-Suevos, D. Rentsch, T. Zimmermann, K. Oksman, *Cellulose* **2010**, *17*, 19.
[67] S. B. Jo, J. Kang, J. H. Cho, *Adv. Sci.* **2021**, *8*, 2004216.
[68] E. M. Bressler, S. Adams, R. Liu, Y. L. Colson, W. W. Wong, M. W. Grinstaff, *Clin. Transl. Med.* **2023**, *13*, 1244.
[69] T. Saito, A. Isogai, *Biomacromolecules* **2004**, *5*, 1983.
[70] J. Schindelin, I. Arganda-Carreras, E. Frise, V. Kaynig, M. Longair, T. Pietzsch, S. Preibisch, C. Rueden, S. Saalfeld, B. Schmid, J. Y. Tinevez, D. J. White, V. Hartenstein, K. Eliceiri, P. Tomancak, A. Cardona, *Nat. Methods* **2012**, *9*, 676.
[71] H. Mary, G. J. Brouhard, (bioRxiv) https://doi.org/10.1101/852772, (accessed: November 2019).